

Experimental Investigation of Boundary Layer Transition on a Swept Flat Plate under Variable Reynolds Number

X. G. Lu^{a,*,**}, S. H. Yi^a, L. He^a, D. D. Gang^a, and H. L. Ding^a

^aNational University of Defense Technology, College of Aerospace Science and Engineering, Changsha, Hunan, China

*e-mail: luxiaoge18@163.com

**e-mail: luxiaoge11@nudt.edu.cn

Received November 23, 2021; revised December 21, 2021; accepted December 21, 2021

Abstract—The experimental study on the transition process of a boundary layer on a 45° swept flat plate is performed in the Mach 6.0 hypersonic low-noise wind tunnel. The instantaneous fine structures of the boundary layer under various Reynolds numbers on the swept flat plate in spanwise planes have been investigated based on the Nano-tracer Planar Laser Scattering (NPLS) technique, respectively. The experimental unit Reynolds number varied from 1.04×10^7 to $2.61 \times 10^7 \text{ m}^{-1}$. The characteristics of spatial-time evolution of the boundary layer translating from laminar to turbulence are analyzed. The results show that with increase in the Reynolds number, the front advance of boundary layer transition on the windward side of the swept flat plate is ahead of schedule, and the transition plane is generally parallel to the leading edge of the 45° swept flat plate. The main reason that turbulence in the boundary layer develops at a short distance is due to the influence of cross-flow. Combined with the cross-flow band structure in NPLS flow visualization images, the characteristics of cross-flow wave are studied, and the influence of cross-flow wave in the boundary layer on boundary layer transition is analyzed.

Keywords: hypersonic, boundary layer transition, swept flat plate, flow visualization, cross-flow

DOI: 10.1134/S0015462822030107

The problem of laminar-turbulent boundary layer transition is the classic problem that has long plagued researchers, and it is also a hot issue in the field of fluid dynamics. The studies of boundary layer transition under hypersonic conditions have great scientific and engineering application value. It is widely used in many engineering applications, such as the engine flow in hypersonic vehicles and the rudder surface flow of hypersonic vehicles. It has an important impact on the key issues of aerodynamics, aerodynamic heat and engine start-up of hypersonic vehicles. In [1] it was pointed out that when the boundary layer changes from laminar to turbulent, the surface frictional resistance and surface heatflux value of the aircraft usually multiply, the friction coefficient and the heat transfer coefficient under turbulent flow conditions are much larger than those in laminar flow. It is generally believed that the flow development state of the boundary layer of the aircraft directly affects the frictional resistance and thermal protection of the aircraft. For the hypersonic aircraft, especially for the flat aircraft, there are many kinds of rudder surfaces or wings with various structures and functions, which can provide the aircraft with high lift-drag ratio, high maneuverability and optimized control scheme, etc. When the aircraft is flying at a high speed, after passing through the incoming hypersonic flow field, its wall boundary layer flow development characteristics and the interference separation between shock wave and boundary layer directly affect the surface thermal and aerodynamic characteristics of rudder surfaces or wings. In the theoretical and experimental research, the rudder and other structures of aircraft are often simplified as swept flat plates for analysis and research.

The boundary layer transition turns to be affected by many factors. In [2] the specific factors that include the level of freedom noise, the bluntness of the leading edge of the object, the flow of the flow, the Mach number, the Reynolds number of the free flow unit, the wall temperature, the angle of attack, the surface roughness of the object, and so on have been summarized. Models such as the swept-wing and swept-plate have achieved some research results under the low-speed conditions. In [3] the investigations of a three-dimensional boundary layer on a 45° swept back flat plate under the condition of artificial disturbances were performed. The initial growth of disturbances was measured by means of hot-wire ane-

mometry. An experimental study of interaction flow induced by a swept blunt fin was presented. However, in high-speed flow, the characteristics of the boundary layer have changed greatly due to the existence of compressible effect, and variables such as the speed, the temperature, and the density have large gradients and complex pulsations, which increase the nonlinearity and randomness of the flow. In [4] the technique of surface heat transfer rate measurement and the schlierenphotos technique were used to study the turbulent interference flow field under the conditions of hypersonic laminar turbulent boundary layer. The experimental study of interaction flow induced by a swept blunt fin was presented. In [5, 6] it has been conducted a detailed experimental study on the effects of the hot line on the stability of the cone and the blunt cone boundary layer and the angle of attack in the hypersonic wind tunnel. However, as the research progressed, it was found that turbulence is not completely random. The discovery of the quasi-ordered structure provides a possibility for study of the turbulence mechanism [7]. However, such researches are still mainly concentrated on the conditions of incompressible flow, while under compressible flow conditions the turbulence structure, the characteristic scale, the intermittency, and the transition mode are different, so a lot of related researches still need to be carried out [8, 9]. For the hypersonic boundary layer in [10] the experimental research was carried out under condition of the Mach number equal to 8.0 using the Rayleigh scattering technique, and the influence of the Reynolds and Mach numbers on the turbulent boundary layer structure was analyzed. It was found that the main factors that affect the turbulent fractal structure and intermittency are the Reynolds number rather than the Mach number. Relatively in a few experimental studies, e.g., in [11, 12], it was pointed out that the main research work in recent years has focused on the development and application of DNS methods for numerical simulation of hypersonic boundary layer flow.

The hypersonic boundary layer on the swept flat plate is characterized by the high Reynolds number, the high Mach number and strong compressibility, and so on. Therefore, the higher requirements are put forward for the technical means of experimental research, and testing means with the higher spatial-temporal resolution are needed for further research. In [13] the experimental study on the interference between the rudder and the flat plate was made by measuring the pressure distribution on the model wall and using the schlieren method. In [14] the instability of turbulent separation induced by blunt leading edge was studied and the low-frequency oscillation characteristics of large-scale structures in the separation region were analyzed. In [15] the planar laser induced fluorescence (PLIF) technique was used to study the separated flow field in the front of the tail with blunt leading edge and the flow field structure and the heat flow distribution characteristics near the rudder surface were obtained. In [16] the experimental and numerical research on the sweepback rudder on the flat plate was carried out, the heat flow distribution on the flat plate surface was measured by liquid crystal thermal imaging technology, and the experimental data with high spatial resolution were obtained. At the same time, the streamline distribution and basic flow results on the wall were obtained by oil flow and schlieren technology, and the experimental results were in good agreement with the numerical simulation results.

Using the traditional optical testing techniques such as the schlieren and shadow ones, it is difficult to achieve fine measurement due to their integral characteristics. Although the Rayleigh scattering (RS) technique in [17, 18] and the PLIF technique in [19, 20] have the higher resolutions, but there are still some defects such as the low signal-to-noise ratio and the complicated calibration method. The particle tracer technique has the characteristics of full-field measurement and the high signal-to-noise ratio. The nano-particle tracer with good followability can realize the measurements of fine structure. The nano-tracer planar laser scattering (NPLS) technique is a flow field fine testing technique independently developed by the author's research group. Its spatial resolution is up to micron, the time resolution is up to 6ns, and the temporal-correlated resolution is up to 200 ns. The test is performed under supersonic flow field. In [21, 22] fruitful results of the research were achieved. In [23] the flow visualization fine structure image of the interference area between the sweepback rudder and the turbulent boundary layer of the incoming flow under the hypersonic condition was obtained using the NPLS technique and the influence of the law of sweepback angle, the rudder slot height and other factors was analyzed in the flow field in front of the rudder, which provided the basis for the optimal design of the rudder surface of the aircraft. In [24] the experimental research on delta wing flat plate was conducted and the fine structure of the wall boundary layer was obtained at different heights from the wall using the NPLS technique.

In the present experiment the transition process of the hypersonic swept flat plate boundary layer is studied and the characteristics of cross-flow waves in the boundary layer are also studied based on NPLS flow visualization images.

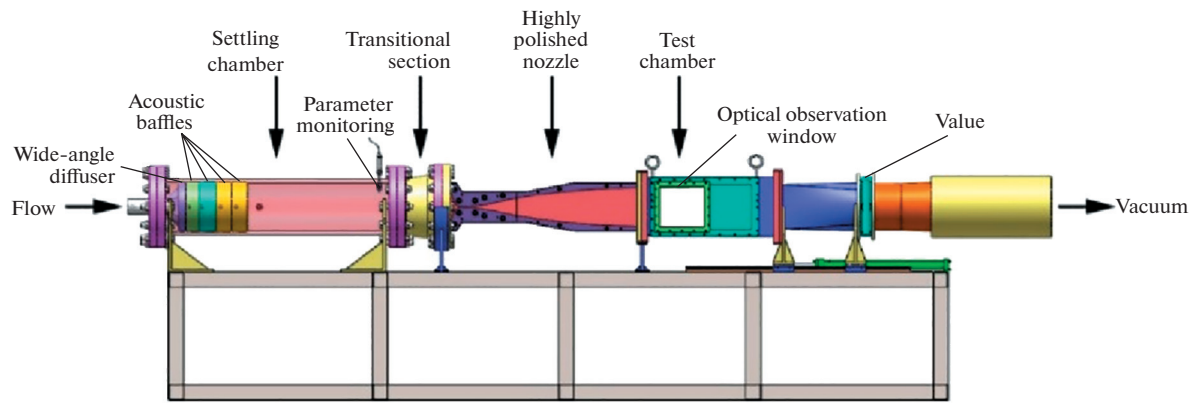


Fig. 1. Photograph of the hypersonic low-noise wind tunnel.

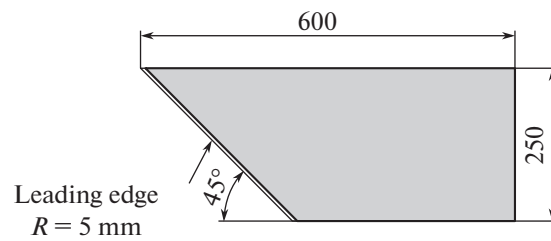


Fig. 2. Photograph of the 45° swept flat plate model.

1. EXPERIMENTAL EQUIPMENT AND TESTING TECHNIQUE

1.1. Hypersonic Low-noise Wind Tunnel and Experimental Model

The experimental study of boundary layer transition on a 45° swept blunt leading edge plate is carried out in the $Ma = 6.0$ hypersonic low-noise wind tunnel (shown in Fig. 1) in the Aerodynamics Laboratory of National University of Defense Technology [25]. The outlet size of the wind tunnel nozzle is 260×260 mm. The length of the experimental section is equal to 600 mm. The unit Reynolds number of the wind tunnel operating ranges from 2.0×10^6 to 5.0×10^7 m^{-1} . The effective running time is more than 30 s, and the Kulite XCE-062-30A high-frequency pulsating pressure sensor is used to calibrate the wind tunnel freedom flow turbulence, and the fluctuation levels is less than 5%. The main parameters of the wind tunnel flow field are shown in Table 1.

The experimental model is a 45° swept flat plate model with a leading edge bluntness of radius 5 mm and the surface roughness of $0.15 \mu m$. The sizes of the model are shown in Fig. 2.

1.2. NPLS System for Hypersonic Wind Tunnels

In Fig. 3 we have reproduced the schematic diagram of the NPLS system [25–27]. It mainly includes an inter-line transmission type double exposure CCD camera, a synchronous controller, a double-cavities Nd : YAG laser, a nanoparticle generator, and a computer system. The resolution of the CCD camera is

Table 1. Flow conditions

Test mode	Ma_∞	T_0 , K	ρ_∞ , $kg\ m^{-3}$	U_∞ , $m\ s^{-1}$	μ , Pa s	Re , m^{-1}
Case I	6.0	450	0.041	891.2	3.43×10^{-6}	1.04×10^7
Case II	6.0	450	0.064	891.2	3.43×10^{-6}	1.67×10^7
Case III	6.0	450	0.080	891.2	3.43×10^{-6}	2.08×10^7
Case IV	6.0	450	0.101	891.2	3.43×10^{-6}	2.61×10^7

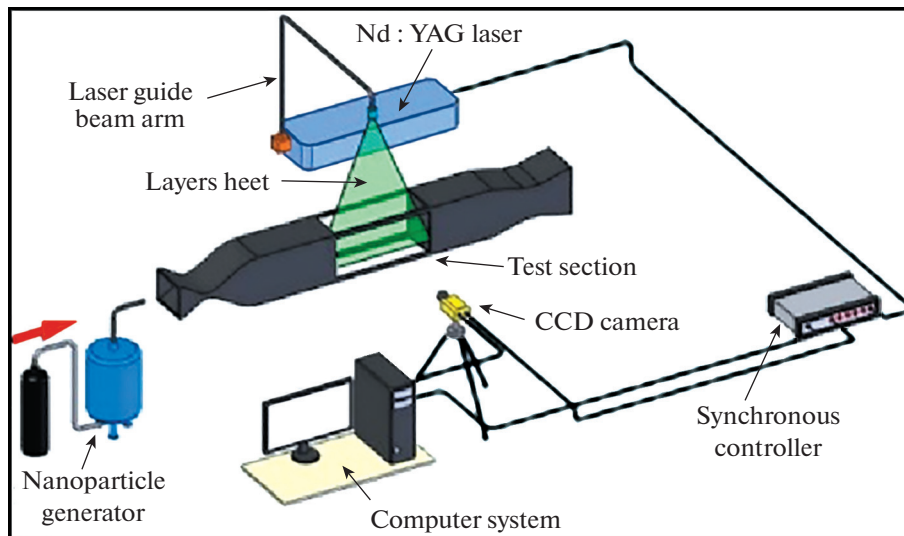


Fig. 3. Schematic of the NPLS experimental system.

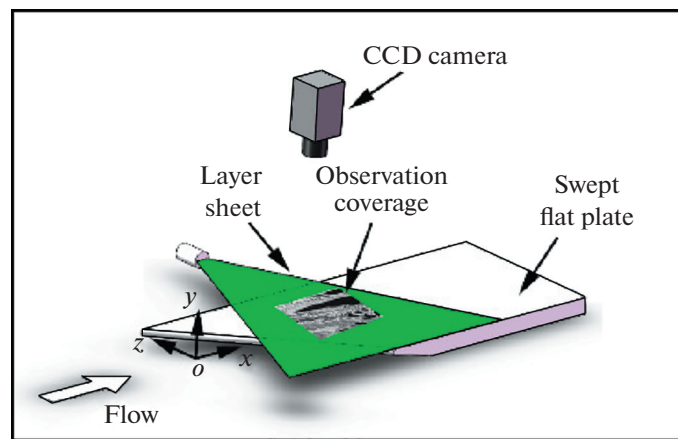


Fig. 4. Schematic of spanwise plane measurement of the swept flat plate model.

2048 × 2048 pixels, the output image gray level is equal to 4096, and the minimum time interval between two images is equal to 200 ns. The laser beam has a wavelength of 532 nm, a single pulse time of 6 ns, a pulse energy of 350 mJ, and the beam waist thickness of less than 1 mm.

2. EXPERIMENTAL RESULTS AND ANALYSIS

2.1. Fine Structure of the Spanwise Plane of the Swept Flat Plate

We will take the Cartesian coordinate system. The intersection of the vertical flow direction and the center surface of the leading edge of the slab front is the coordinate system origin (o point), the flow direction is the positive direction of the x -axis, and the vertical swept flatplate plane is upward for the positive direction of the y -axis, the direction perpendicular to the x - y plane pointing to the starting point of the swept plate is the positive direction of the z -axis, and the x - z plane is the boundary layer spanwise plane. Figure 4 is a schematic of the experimental layout of the measurement in the spanwise plane.

In Figs. 5a–5h we have shown the NPLS images of the spanwise plane boundary layer structure of a smooth flat plate model with the swept blunt leading edge at various Reynolds numbers and the model angle of attack $\alpha = 0^\circ$. The spatial resolution of all images is equal to 69 $\mu\text{m}/\text{pixel}$, and the flow is directed from left to right. The field of view of the image is in the center plane of the swept flat plate with $x = 110$ –270 mm, and the shooting range of spanwise plane is equal to $Z = -50$ –80 mm. In Table 1 the heights of

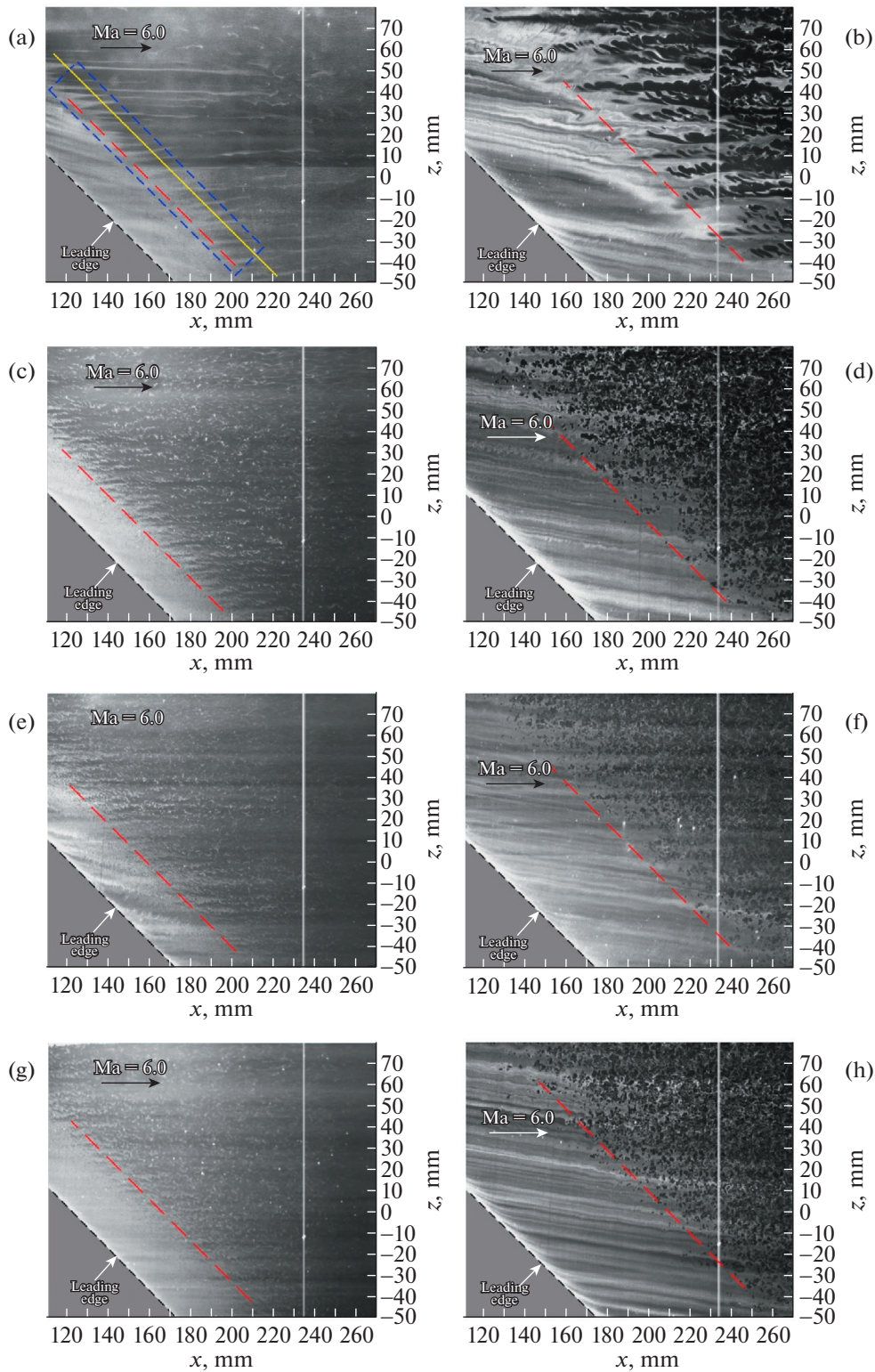


Fig. 5. Flow structure on a swept flat plate spanwise plane under case I– case IV. (a) Case I: $Re = 1.04 \times 10^7 \text{ m}^{-1}$, $y = 1.2 \text{ mm}$; (b) Case II: $Re = 1.04 \times 10^7 \text{ m}^{-1}$, $y = 2.5 \text{ mm}$; (c) Case III: $Re = 1.67 \times 10^7 \text{ m}^{-1}$, $y = 1.2 \text{ mm}$; (d) Case IV: $Re = 1.67 \times 10^7 \text{ m}^{-1}$, $y = 2.5 \text{ mm}$; (e) Case III: $Re = 2.08 \times 10^7 \text{ m}^{-1}$, $y = 1.2 \text{ mm}$; (f) Case III: $Re = 2.08 \times 10^7 \text{ m}^{-1}$, $y = 2.5 \text{ mm}$; (g) Case IV: $Re = 2.61 \times 10^7 \text{ m}^{-1}$, $y = 1.2 \text{ mm}$; (h) Case IV: $Re = 2.61 \times 10^7 \text{ m}^{-1}$, $y = 2.5 \text{ mm}$.

the image laser sheet from the upper surface of the swept flat plate under each test mode are equal to $y = 1.2$ and 2.5 mm, respectively. There are white vertical lines near $x = 235$ mm in the spanwise flow visualization image, which were caused by the sudden supersaturation of the image during the experiment, which leads to the pixel damage of CCD camera, and the image was directly displayed as a white area. But this area does not affect the analysis of experimental data, so this part of bad data was not removed in the actual process of data processing. It can be seen from all the images in Figs. 5a–5h that for the flat plate model with the swept blunt leading edge, the boundary layer transition front on the wall is basically parallel to the swept leading edge of the swept flat plate, and obvious laminar flow bands can be observed at low Reynolds numbers, such as: case I, case II, and case III.

The experimental unit Reynolds number of the images in Figs. 5a and 5b is equal to $1.04 \times 10^7 \text{ m}^{-1}$. It can be seen from the images that when the height of laser sheet is equal to $y = 1.2$ mm, obvious laminar flow bands can be seen in the boundary layer of the swept flat plate in the measurement area. The parallel distance between the leading edge of laminar flow bands and the swept leading edge is equal to 26.9 mm, and obvious laminar flow bands and partial turbulence structures can be seen in the rear measurement area. However, the boundary layer has not completely developed into a turbulent boundary layer. It is generally believed that the boundary layer transition on the swept flat plate is greatly affected by cross flow, and the strip structure ahead of it completely develops into turbulent boundary layer is considered as cross flow strip, that is, cross flow wave. According to the measurement of the strip position in the image, the angle between the cross-flow wave and the swept leading edge in Fig. 5a is about 42.8° . When the height of laser sheet is equal to $y = 2.5$ mm, the flow field structure cannot be seen in the front area of the model, as shown in Fig. 5b. It is because the boundary layer at the front of the model is still in laminar flow state, and the height of $y = 2.5$ mm has exceeded the thickness of the laminar boundary layer, so there is no flow structure in the white area. From Fig. 5b only a part of the turbulent flow structure can be seen in the rear section of the test area. From the point of view of flow structure, the swept flat boundary layer in the measurement area also has obvious strip characteristics along the flow direction. However, due to the higher height of laser sheet light, a part of the measurement area has exceeded the thickness of the boundary layer, and less boundary layer information can be seen. Moreover, what is seen in the image is not like the regular strip structure as shown in Fig. 5a, but a vortex structure with three-dimensional characteristics.

The experimental unit Reynolds number of the images in Figs. 5c and 5d is equal to $1.67 \times 10^7 \text{ m}^{-1}$. It can be seen from the images that when the height of laser sheet is equal to $y = 1.2$ mm, obvious transition structure can be seen in the swept flat boundary layer in the measurement area, and laminar flow zone, large-scale vortex structure and completely broken small vortex structure can be clearly seen. A short-distance cross-flow strip can also be seen ahead of the transition zone, and the parallel distance between the leading edge of the cross-flow strip and the swept leading edge is equal to 19.8 mm. When the height of the laser sheet is equal to $y = 2.5$ mm, the large eddy structure after transition can be seen in the swept flat boundary layer in the measurement area. However, as the height of laser sheet becomes higher, only the region after boundary layer transition can be seen in the image, and the laminar structure can no longer be seen in the observed region.

The experimental unit Reynolds number of the images in Figs. 5e and 5f is equal to $2.08 \times 10^7 \text{ m}^{-1}$. It can be seen from the images that the boundary layer can transit from laminar to turbulent flow when the height of the laser sheet is equal to $y = 1.2$ mm and the observed parallel distance between the front edge of the flow field region and the swept front edge is equal to 30.4 mm. Compared with the transition zone at the same height with the unit Reynolds number of $1.67 \times 10^7 \text{ m}^{-1}$, the distance between the front of the flow field structure and the swept front edge increases, which is because the thickness of the boundary layer corresponding to the wall density gradually becomes thinner after the Reynolds number increases. Therefore, at the same height, the blank area in front of the transition zone increases relatively and less flow field information can be seen. The laminar flow area at the front of the transition zone can not be clearly distinguished. When the height of the laser sheet is equal to $y = 2.5$ mm, it can be seen that the vortex broken structure is obvious at the rear of the swept flat plate, but no obvious flow structure is observed at the front region. As compared with the low Reynolds number, the vortex structure in the measurement region is more broken, which indicates that the boundary layer transition region is fully developed into turbulence after the Reynolds number increases.

The experimental unit Reynolds numbers of the images in Figs. 5g and 5h are equal to $2.61 \times 10^7 \text{ m}^{-1}$. From the images, it can be seen that the parallel distance between the front edge of the observed flow field area and the swept front edge is equal to 33.9 mm when the height of the laser sheet is equal to $y = 1.2$ mm, and the vortex structure is more broken when the height of the laser sheet is equal to $y = 2.5$ mm. Although the transition position of boundary layer is much earlier, because the thickness of boundary layer

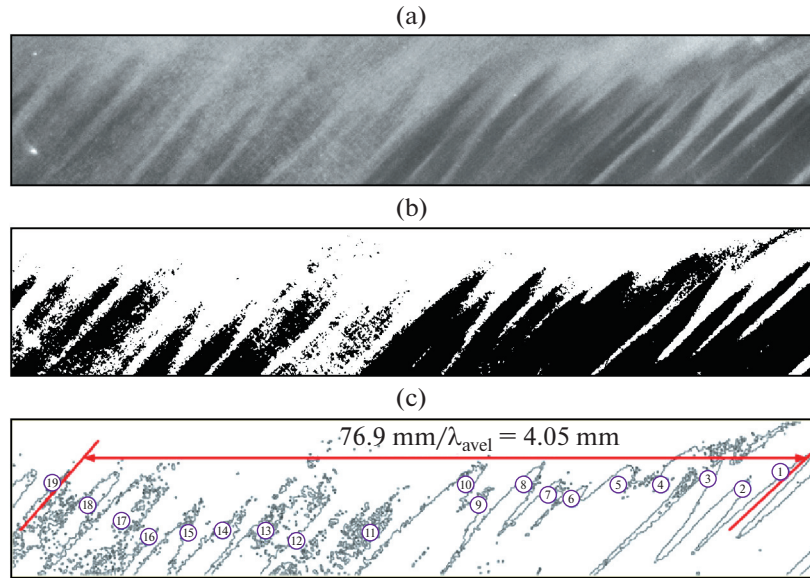


Fig. 6. Cross-flow wave analysis of the swept blunt leading edge plate ($Re = 1.04 \times 10^7 \text{ m}^{-1}$). (a) Original NPLS image (Enlarged image of the partial cross-flow strip in Fig. 5a). (b) Binary image of Fig. 6a. (c) The result of edge detection of Fig. 6b.

is thinner, the information of vortex structure can be seen less than when Reynolds number is equal to $2.08 \times 10^7 \text{ m}^{-1}$.

2.2. Analysis of Cross-flow Characteristics on the Swept Flat Plate Based on NPLS Images

For the swept flat plate, boundary layer transition is obviously affected by cross-flow. According to the cross-flow band appearing in the spanwise plane flow visualization images at the angle of attack $\alpha = 0^\circ$ of the swept flat plate with blunt leading edge, the characteristics of cross-flow wave in some images are extracted and analyzed separately in this paper.

According to the experimental results in the spanwise plane shown in Figs. 5a–5h, in Fig. 6 we have analyzed the cross-flow waves in the spanwise plane based on the NPLS experimental results on the swept blunt leading edge smooth plate model with the experimental unit Reynolds number equal to $1.04 \times 10^7 \text{ m}^{-1}$ and the model angle of attack $\alpha = 0^\circ$. Figure 6a represents an enlarged image of the some cross-flow strips in the blue dashed box in Figs. 5a and 6b is an image after binarization of the image extracted in Fig. 6a. According to the obtained binary image, edge detection is used to obtain a finer outer contour structure of the cross-flow strip, as shown in Fig. 6c. According to the spatial resolution of image acquisition, it can be calculated that the spatial distance between the center lines of two cross-flow strips marked by red solid lines in Fig. 6c is equal to $L_1 = 76.9 \text{ mm}$. According to the image identification of Fig. 6c after edge detection, the number of cross-flow bands in the selected interval is marked in the image ($n_1 = 19$), and the average wavelength of cross-flow wave under this working condition is equal to $\lambda_{\text{ave1}} = L_1/n_1 = 4.05 \text{ mm}$ according to statistical calculation.

Figure 7 also shows the edge detection results obtained from two frames of NPLS images related to Fig. 6a, in which the black edge image is the result at t_0 and the red edge image is the result at $t_0 + 5 \mu\text{s}$. It can be seen from the results in Fig. 7 that within a time interval of $5 \mu\text{s}$, the cross-flow wave structure mainly translates downstream along the flow direction, and the spanwise deformation is very small. According to the displacement of several cross-flow strips within the time-dependent, the overall moving distance of the cross-flow wave is equal to $S_1 = 0.4 \text{ mm}$, from which the propagation speed of the cross-flow wave can be calculated to be equal to $v_1 = 80 \text{ m/s}$, and the statistical wavelength of the cross-flow wave calculated from the previous calculation is equal to $\lambda_{\text{ave1}} = 4.05 \text{ mm}$, which can be calculated by formula (2.1), and the characteristic frequency of the development of the cross-flow wave is equal to $f_1 = 19.7 \text{ kHz}$.

$$f = \frac{v}{\lambda}. \quad (2.1)$$

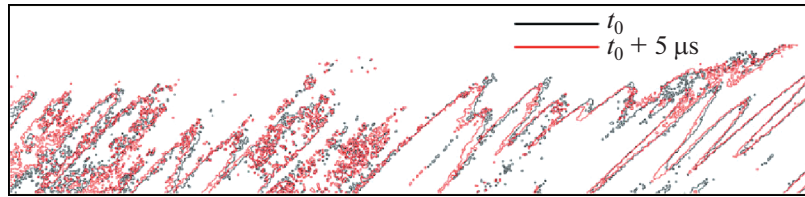


Fig. 7. Time-dependent image analysis of the swept blunt leading edge plate ($Re = 1.04 \times 10^7 \text{ m}^{-1}$).

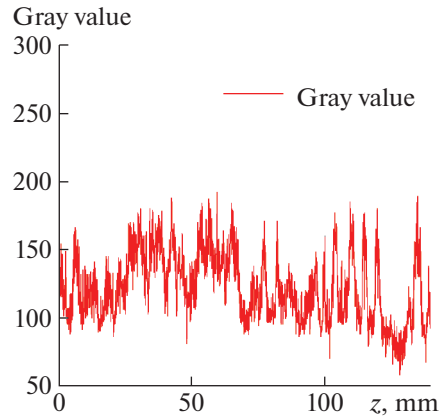


Fig. 8. Gray value extraction of the swept blunt leading edge plate ($Re = 1.04 \times 10^7 \text{ m}^{-1}$).

In the time interval of $\Delta t = 5 \mu\text{s}$, the cross-flow vortex is mainly translated, and the structural deformation is small. According to the Taylor hypothesis, it can be considered that the cross-flow wave structure only translates in a very short time, and the density change characteristics can be reflected according to the gray value of the image. In order to study the frequency domain characteristics of the cross-flow wave based on the flow visualization image, the gray value of the image is extracted along the yellow solid line in Fig. 5a, and the gray curve as shown in Fig. 8 is obtained. According to the spatial gray distribution and the average velocity of cross-flow wave translation calculated above, the gray coordinates are converted to obtain the pulsation curve of image gray in a short time as shown in Fig. 9. The distribution of power spectral density is obtained by power spectral calculation. As shown in Fig. 10, the characteristic frequency of cross-flow wave can be read from the power spectral data at 23.7 kHz, which is similar to the result directly calculated by image recognition, that is, the cross-flow characteristics can be studied based on the NPLS images.

The flow visualization images in Figs. 5c and 5e at the Reynolds numbers equal to 1.67×10^7 and $2.08 \times 10^7 \text{ m}^{-1}$, respectively, are analyzed in the same way as the image processing in Fig. 5a. According to the calculation results on the swept flat plate with blunt leading edge, when the experimental Reynolds number is equal to $1.67 \times 10^7 \text{ m}^{-1}$, the overall moving distance of the cross-flow wave is equal to $S_{II} = 2.01 \text{ mm}$, from which the propagation speed of the cross-flow wave can be calculated to be equal to $v_{II} = 402 \text{ m/s}$. According to the statistical wavelength of the cross-flow wave calculated to be equal to $\lambda_{\text{aveII}} = 4.7 \text{ mm}$, the characteristic frequency of the cross-flow wave development can be calculated to be equal to $f_{II} = 85.5 \text{ kHz}$. When the experimental Reynolds number is $2.08 \times 10^7 \text{ m}^{-1}$, the overall moving distance of the cross-flow wave is equal to $S_{III} = 2.64 \text{ mm}$, from which the propagation speed of the cross-flow wave can be calculated as $v_{III} = 528 \text{ m/s}$, and according to the statistical wavelength of the cross-flow wave calculated as $\lambda_{\text{aveIII}} = 4.75 \text{ mm}$, the characteristic frequency of the cross-flow wave development can be calculated as equal to $f_{III} = 111.2 \text{ kHz}$. Compared with the experimental Reynolds number of $1.04 \times 10^7 \text{ m}^{-1}$, with increase in the Reynolds number, the distance between cross-flow strips increased slightly, and the number of cross-flow strips per unit length decreases, that is, the statistical wavelength of corresponding cross-flow strips increased, the propagation speed of cross-flow waves increased obviously, and the corresponding characteristic frequency also increases.

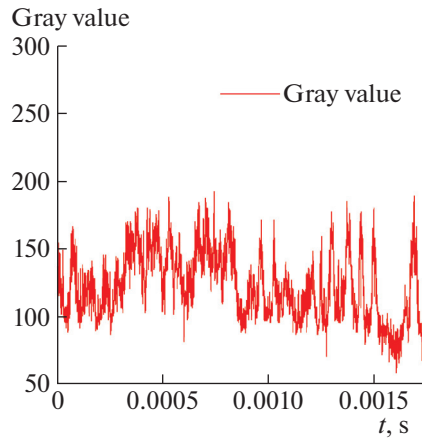


Fig. 9. Time domain signal of the gray value of swept blunt leading edge plate ($Re = 1.04 \times 10^7 \text{ m}^{-1}$).

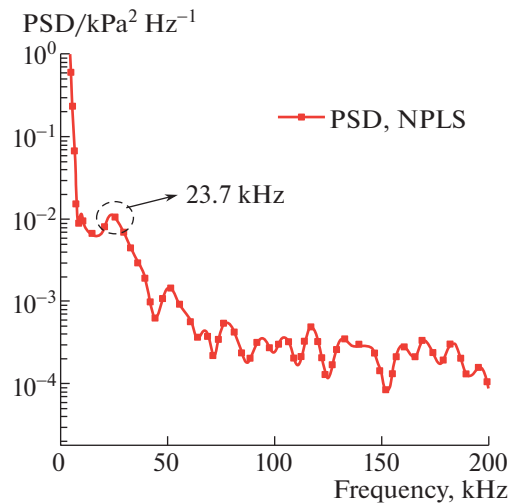


Fig. 10. Power spectrum of gray value of swept blunt leading edge plate ($Re = 1.04 \times 10^7 \text{ m}^{-1}$).

SUMMARY

In this paper, the high-resolution images of the flat boundary layer with swept blunt leading edge developed from laminar flow to turbulent flow were obtained under variable Reynolds number by using the high-time and spatial resolution flow field measurement and visualization technique (NPLS technique). The fine structure of the flow field during the development of the boundary layer was obtained, thus, the research on the mechanism and law of boundary layer transition is completed. According to the experimental results of NPLS, the boundary layer transition front on smooth flat plate with swept blunt leading edge is parallel to the leading edge of swept flat plate. Moreover, obvious cross-flow bands can be seen at low Reynolds number at the attack angle of 0° , but no band structure can be observed when Reynolds number increases to a certain value. At the same angle of attack, with increase in the Reynolds number, the transition position of boundary layer on windward side is advanced. Through the analysis of cross-flow strips in the span wise images of NPLS with Reynolds number ranging from 1.04×10^7 to $2.08 \times 10^7 \text{ m}^{-1}$ at zero angle of attack, under this working condition, the wavelength range of cross-flow wave is from 4.05 to 4.75 mm, and the corresponding frequency range of cross-flow wave is from 19.7 to 111.2 kHz. With increase in the Reynolds number, the distance between cross-flow strips increases slightly, and the number of cross-flow strips per unit length decreases, that is, the statistical wavelength of corresponding cross-flow strips increases, the propagation speed of cross-flow waves increases obviously, and the corresponding characteristic frequency also increases.

FUNDING

The work was supported by the National Key Research and Development Plan of China (Grant no. 2019YFA0405300) and the Major Research Plan of the National Natural Science Foundation of China (Grants nos. 91752102 and 11832018) and the National Project for Research and Development of Major Scientific Instruments of China (Grant no. 11527802). This support is gratefully acknowledged.

REFERENCES

1. Liu, X.L., Yi, S.H., Niu, H.B., and Lu, X.G., Influence of laser-generated perturbations on hypersonic boundary-layer stability, *Acta Phys. Sin.*, 2018, vol. 67, no. 21.
2. Zhong, X.L., Direct numerical simulation of 3-D hypersonic boundary layer receptivity to freestream disturbances, in: *The 36th AIAA Aerospace Sciences Meeting and Exhibit*, American Institute of Aeronautics and Astronautics, 1998.
3. Wu, Y.J. and Ming, X., Experimental Study of Initial Disturbance Growth for Cross Flow Instability, *ACTA-AerodynamicaSinica*, 2000, vol. 18, no. 1, pp. 62–67.
4. Li, S.X., Ma, J.K., and Guo, X.G., Experimental study of hypersonic interaction flow induced by high sweep fin model, *Phys. of Gases*, 2016, vol. 1, no. 3, pp. 1–5.
5. Stetson, K.F., Thompson, E.R., Donaldson, J.C., and Siler, L.G., Laminar boundary layer stability experiments on a cone at Mach 8, Part 1: Sharp cone, *AIAA Paper 83-1761*, 1983.
6. Stetson, K.F., Thompson, E.R., Donaldson, J.C., and Siler, L.G., Laminar boundary layer stability experiments on a cone at Mach 8, Part 2: Blunt cone, *AIAA Paper 84-0006*, 1984.
7. Kline, S.J., Reynolds, W.C., Schranb, F.A., and Runstadler, P.W., The structure of turbulent boundary layer, *J. Fluid Mech.*, 1967, vol. 30, no. 4, pp. 741–774.
8. Theodorsen, T., Mechanism of turbulence, in: *Proceedings of the second Midwestern conference on fluid mechanics*, Ohio State University, USA, 1952.
9. Head, M.R. and Bandyopadhyay, P.R., New aspects of turbulent boundary-layer structure, *J. Fluid Mech*, 1981, vol. 107, pp. 297–338.
10. Baumgartner, M.L., Erbland, P.J., Etz, M.R., Yalin, A.B., Muzas, K., Smits, A.J., Lempert, W.R., and Miles, R.B., Structure of a Mach 8 turbulent boundary layer, in: *35th Aerospace Sciences Meeting & Exhibit Reno, NV*, 1997.
11. Martin, M.P., Direct numerical simulation of hypersonic turbulent boundary layers. Part 1. Initialization and comparison with experiments, *J. Fluid Mech*, 2007, vol. 570, pp. 347–364.
12. Li, X.L., Fu, D.X., and Ma, Y.W., Assessment of the compressible turbulence model by using the DNS data, *Chin. J. Theor. Appl. Mech.*, 2012, vol. 44, no. 2.
13. Li, Y.L. and Li, S.X., Investigation of interactive hypersonic laminar flow over blunt fin, *J. Astron.*, 2007, vol. 28, no. 6, pp. 1472–1477.
14. Wang, S.F. and Wang, Y., Turbulent separation features induced by blunt fins in hypersonic flow, *Acta Aeronautica et AstronauticaSinica*, 1996, vol. 17, no. 7, pp. 2–7.
15. Fox, J.S., O’Byrne, S., and Houwing, A.P., Fluorescence visualization of hypersonic flow establishment over a blunt fin, *AIAA J.*, 2001, vol. 39, no. 7, pp. 1329–1337.
16. Tutty, O.R., Roberts, G.T., and Schuricht, P.H., High-speed laminar flow past a fin–body junction, *J. Fluid Mech.*, 2013, vol. 737, pp. 19–55.
17. Smith, M.W. and Smits, A.J., Visualization of the structure of supersonic turbulent boundary layers, *Exper. in Fluids*, 1995, vol. 18, no. 4, pp. 288–302.
18. Smith, M.W., Smits, A.J., and Miles, R.B., Cinematic visualization of coherent density structures in a supersonic turbulent boundary layer, *Opt. Lett.*, 1988, p. 14916.
19. Danehy, P.M., Wilkes, J.A., Alderfer, D.W., Jones, S.B., Robbins, A., Patry, D., and Schwartz, R., Planar laser-induced fluorescence (PLIF) investigation of hypersonic flow fields in a Mach 10 wind tunnel, *AIAA Paper*, 2006, pp. 2006–3442.
20. Bathel, B.F., Danehy, P.M., Inman, J.A., David, A., and Scott, B., PLIF visualization of active control of hypersonic boundary layers using blowing, *AIAA Paper*, 2008, pp. 2008–4266.
21. He, L., Yi, S.H., Tian, L.F., Chen, Z., and Zhu, Y.Z., Simultaneous density and velocity measurements in a supersonic turbulent boundary layer, *Chin. Phys.*, 2013, vol. 22, no. 2, pp. 328–334.
22. Zhu, Y.Z., Yi, S.H., Chen, Z., Ge, Y., Wang, X.H., and Fu, J., Experimental investigation on aero-optical aberration of the supersonic flow passing through an optical dome with gas injection, *Acta Phys. Sin.*, 2013, no. 8, pp. 259–266.
23. Gang, D.D., Low noise experimental investigation on supersonic/hypersonic boundary layer transition and flow over blunt fins, Changsha: National University of Defense Technology, 2017.
24. Niu, H.B., Yi, S.H., Liu, X.L., Lu, X.G., and Gang, D.D., Experimental investigation of boundary layer transition over a delta wing at $Ma = 6$, *Chin. J. Aeronaut.*, 2020, vol. 33, no. 7, pp. 1889–1902.
25. Lu, X.G., Yi, S.H., He, L., Liu, X.L., and Niu, H.B., Experimental investigation of the hypersonic boundary layer transition on a 45° swept flat plate, *Fluid Dyn.*, 2020, vol. 55, no. 1, pp. 111–120.
26. Zhao, Y.X., Yi, S.H., Tian, L.F., and Cheng, Z.Y., Supersonic flow imaging via nanoparticles, *Sci. China, Ser. E*, 2009, vol. 52, no. 12, pp. 3640–3648.
27. He, L., Yi, S.H., and Lu, X.G., Experimental study on the density characteristics of a supersonic turbulent boundary layer, *Acta Phys. Sin.*, 2017, vol. 66, no. 2, p. 025701.